

A Deep Learning Approach to Resolve Aliasing Artifacts in Ultrasound Color Flow Imaging

Hassan Nahas, *Graduate Student Member, IEEE*, Jason S. Au¹, *Member, IEEE*, Takuro Ishii², *Member, IEEE*, Billy Y. S. Yiu³, *Member, IEEE*, Adrian J. Y. Chee, *Member, IEEE*, and Alfred C. H. Yu⁴, *Senior Member, IEEE*

Abstract—Despite being used clinically as a noninvasive flow visualization tool, color flow imaging (CFI) is known to be prone to aliasing artifacts that arise due to fast blood flow beyond the detectable limit. From a visualization standpoint, these aliasing artifacts obscure proper interpretation of flow patterns in the image view. Current solutions for resolving aliasing artifacts are typically not robust against issues such as double aliasing. In this article, we present a new dealiasing technique based on deep learning principles to resolve CFI aliasing artifacts that arise from single- and double-aliasing scenarios. It works by first using two convolutional neural networks (CNNs) to identify and segment CFI pixel positions with aliasing artifacts, and then it performs phase unwrapping at these aliased pixel positions. The CNN for aliasing identification was devised as a U-net architecture, and it was trained with *in vivo* CFI frames acquired from the femoral bifurcation that had known presence of single- and double-aliasing artifacts. Results show that the segmentation of aliased CFI pixels was achieved successfully with intersection over union approaching 90%. After resolving these artifacts, the dealiased CFI frames consistently rendered the femoral bifurcation's triphasic flow dynamics over a cardiac cycle. For dealiased CFI pixels, their root-mean-squared difference was 2.51% or less compared with manual dealiasing. Overall, the proposed dealiasing framework can extend the maximum flow detection limit by fivefold, thereby improving CFI's flow visualization performance.

Index Terms—Aliasing, color flow imaging (CFI), deep learning, Doppler ultrasound, U-net.

I. INTRODUCTION

COLOR flow imaging (CFI) [1] has long been a popular modality for noninvasive mapping of blood flow *in*

Manuscript received May 5, 2020; accepted June 7, 2020. Date of publication June 10, 2020; date of current version November 23, 2020. This work was supported in part by Natural Sciences and Engineering Council of Canada under Grant (CREATE-528202-2019, RGPIN-2016-04042), Canadian Institutes of Health Research (PJT-153240), Canada Foundations for Innovation (36138), and Ontario Early Researcher Award (ER16-12-186). (Corresponding author: Alfred C. H. Yu.)

Hassan Nahas, Billy Y. S. Yiu, Adrian J. Y. Chee, and Alfred C. H. Yu are with the Schlegel Research Institute for Aging, University of Waterloo, Waterloo, ON N2L 3G1, Canada, and also with the Department of Electrical and Computer Engineering, University of Waterloo, Waterloo, ON N2L 3G1, Canada (e-mail: alfred.yu@uwaterloo.ca).

Jason S. Au is with the Department of Kinesiology, University of Waterloo, Waterloo, ON N2L 3G1, Canada.

Takuro Ishii is with the Frontier Research Institute for Interdisciplinary Sciences, Tohoku University, Sendai 980-8578, Japan.

This article has supplementary downloadable material available at <https://ieeexplore.ieee.org>, provided by the author.

Digital Object Identifier 10.1109/TUFFC.2020.3001523

in vivo [2]. It is particularly relevant to cardiovascular healthcare where CFI can be used to detect stenosis [3] and to monitor plaque formation through identifying abnormal flow phenomena, such as jets, turbulence, and flow reversal [1], [4]. However, CFI is known to be prone to aliasing artifacts that arise when the mean axial flow velocity at certain pixel positions exceeds the detectable limit [5]. Such aliasing artifacts are fundamentally attributed to systemic limitations in its data acquisition paradigm, in which slow-time pulse-echo sampling is performed at each pixel position. Aliasing occurs whenever the pulse repetition frequency (PRF) used for slow-time sampling at each pixel position falls below the minimum rate (i.e., the Nyquist limit) needed to acquire an adequately sampled slow-time signal, whose mean Doppler frequency supposedly should correspond to the local average axial flow velocity according to the Doppler equation [5]. If aliasing is present at a pixel position, its resulting CFI pixel value would become misleading in different ways for the typical color encoding scheme that uses a red-blue bicolor hue to indicate the estimated mean velocity. First, the mapped color at a pixel position may be flipped to its complementary hue (i.e., from red to blue, or vice versa), thereby falsely indicating a change in the flow direction. Second, the mapped color may fall within a less saturated part of the same hue such that a fast flow speed is deceptively rendered as slower flow in the same direction.

From a visualization standpoint, the presence of aliased color pixels in a CFI frame is known to jeopardize the proper interpretation of flow patterns in the image view. Indeed, in the presence of a curvy vessel geometry, the rendered CFI flow pattern often looks like a color mosaic even without aliasing [6]. Thus, if some aliased color pixels are present, gaining an intuitive understanding of the rendered flow profile becomes an extremely challenging task. Note that, from a flow quantification perspective, aliasing is an issue that affects the fidelity of not only CFI but also vector Doppler that seeks to compute both axial and lateral velocity components [7], [8]. For the latter method, if flow vectors cannot be estimated accurately, they would not yield vector flow images with consistent visualization of the true flow profile [9]. Such an issue, in turn, would make it difficult to properly use the vector Doppler approach to effectively interpret complex flow dynamics that frequently appear in diseased vessels [10]–[12].

To resolve aliasing artifacts in CFI data processing, several methods and algorithms have been proposed in the

literature [13], [14]. For instance, an extended autocorrelation method has been proposed to double the maximum measurable velocity limit [15]. Also, a staggered data acquisition sequence may be used to perform aliasing-free CFI below the Nyquist limit [16]. These methods fundamentally involve changes to the system's front-end operations. Alternatively, aliasing artifacts may be tackled through image processing principles. For this type of dealiasing algorithm, a two-step process is commonly adopted: 1) identification and segmentation of aliased pixels and regions in the CFI frame, and 2) correction of aliasing errors at the identified pixel positions based on flow profile properties. Accordingly, solutions based on fuzzy logic [17] and unsupervised segmentation [18] have been proposed. These image-based dealiasing methods have succeeded in mitigating single-aliasing errors, which correspond to cases when the actual Doppler frequency f' exceeds the maximum unaliased frequency f_{\max} by up to onefold of the unaliased frequency range (i.e., $f_{\max} < f' < 3f_{\max}$, given that the unaliased frequency range equals to $f_{\max} - f_{\min} = 2f_{\max}$). However, they are not effective in handling the more challenging double-aliasing cases, which occur when f' exceeds f_{\max} by an amount between onefold and twofold of the unaliased frequency range; i.e., $3f_{\max} < f' < 5f_{\max}$) [18]. A more robust dealiasing technique is yet needed for CFI applications.

In this article, we present a new dealiasing framework that is based on deep learning principles to suppress aliasing artifacts in CFI frames. We posit that aliased pixel positions and regions in a CFI frame can be effectively segmented by devising a convolutional neural network (CNN) that is trained to identify both single- and double-aliasing cases. We also posit that these aliased pixels may be subsequently removed via phase unwrapping. In approaching the CNN design, we have investigated the applicability of different ultrasound signal features as learning input for the CNN to segment aliased pixels in CFI frames. These features included data types derived from both the Doppler spectral contents and flow speckle patterns.

Our dealiasing framework is built upon the recent success of CNNs in the domain of semantic segmentation [19], in which fully-convolved neural networks have been successfully applied to a variety of data sets [20]. More specifically, our framework makes use of a class of CNN architectures known as encoder–decoder [21], which has demonstrated superior performance in the segmentation of biomedical images [22], [23]. An encoder–decoder CNN is known to be potent in extracting and combining translation-invariant patterns at multiple scales [24], and these identified patterns can be refined to achieve high-resolution segmentation through skip connections [25]. This type of CNN is seemingly suitable for aliased pixel segmentation that may require information from a large neighborhood to disambiguate. Indeed, in a recent preliminary study [26], we have demonstrated the initial feasibility of devising an encoder–decoder CNN for single-aliasing detection *in vitro*. Here, we shall expand the framework to address practical CFI scenarios *in vivo* that may include single aliasing and double aliasing.

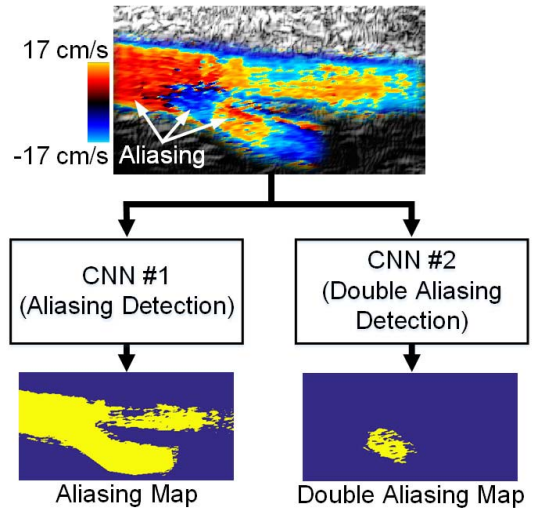


Fig. 1. Use of two CNNs for aliasing detection in ultrasound CFI. CNN #1 is for the general segmentation of aliased pixels, which may include single aliasing and double aliasing. CNN #2 is specifically for the segmentation of double aliasing.

II. THEORETICAL PRINCIPLES

A. Overall Framework for Aliasing Segmentation

Our strategy for the identification of aliased pixels in ultrasound CFI was based on the use of two CNNs. As shown in Fig. 1, CNN #1 was trained to detect aliased pixels (both single aliasing and double aliasing) in CFI frames, while CNN #2 was trained to specifically segment double-aliasing cases. The second CNN was needed in this work in order to facilitate the adaptive correction of double-aliasing artifacts (to be discussed in Section II-E). The training was done according to supervised learning principles, for which labeled data sets were generated.

B. Training Features for Aliasing Identification

To successfully apply supervised learning to aliased CFI pixel identification, it is important to identify the relevant ultrasound information (or features) that can be used as training input. In this work, five different types of image-based data sets, as obtained from different steps in the CFI data processing pipeline as illustrated in Fig. 2, were used to train CNNs for aliasing detection. These data features include: 1) Doppler frequency; 2) Doppler power; 3) Doppler bandwidth; 4) flow speckle speed; and 5) flow speckle motion angle. For each image-based data set, every pixel denoted the value of that data feature at the corresponding location in the image view. Further details on each training data type are given as follows.

1) *Doppler Frequency*: Aliasing typically emerges in CFI as abrupt disruptions and irregularities in the rendered color map in the image view. Since CFI maps are after all color-encoded maps of the mean Doppler frequencies, the spatial distribution of the mean Doppler frequency values is an obvious data type to include for the training of an aliasing detection CNN. In this study, the mean Doppler frequency \hat{f} at each pixel position was calculated using the Kasai estimator [27]

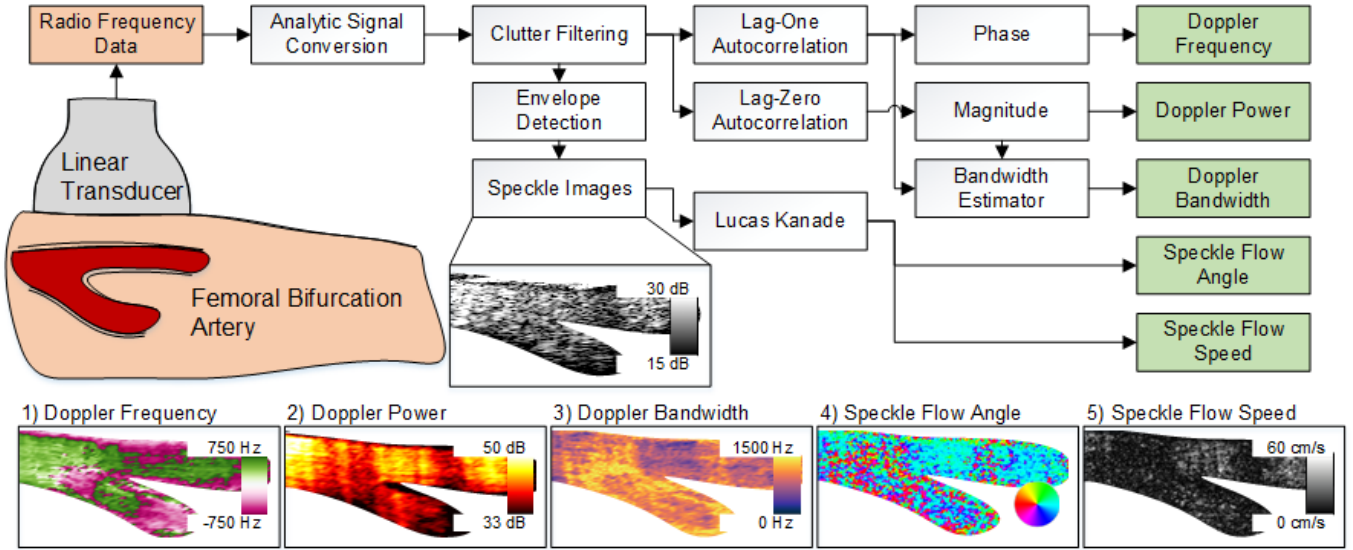


Fig. 2. Data features used for CNN training: 1) Doppler frequency; 2) Doppler power; 3) Doppler bandwidth; 4) speckle flow angle; and 5) speckle flow speed. These features are derived from different parts of the CFI signal processing pipeline. Optical flow analysis was performed to derive flow speckle patterns.

(the phase of the lag-one autocorrelation function), as it is the standard algorithm used in clinical scanner development. \hat{f} can be calculated as follows:

$$\hat{f} = \frac{\text{PRF}}{2\pi} \angle R_s(1) \text{ for } R_s(l) = \sum_{n=1}^{N-l} s^*[n]s[n+l] \quad (1)$$

where $s[n]$ is the n th sample in the slow-time ensemble (which is an analytic signal), N is the ensemble size, $R_s(l)$ is the autocorrelation function at lag l , and \angle denotes the phase of a complex data value.

2) Doppler Power: The clutter-filtered power Doppler map is often used to identify the presence of flow in the image view, and thus, it could be useful for differentiating between tissue, flow, and noise. As such, the spatial distribution of the Doppler power values may serve as complementary input for aliasing prediction. Each Doppler power value \hat{p} is simply the mean power of the slow-time ensemble after clutter filtering

$$\hat{p} = \frac{|R_s(0)|}{N}. \quad (2)$$

3) Doppler Bandwidth: Aliasing, especially at higher orders, can impact the Doppler bandwidth through smearing the Doppler spectrum, thereby resulting in high bandwidth values. Accordingly, the Doppler bandwidth may be another useful predictor of aliasing artifact. Based on the Kasai algorithm [27], this quantity can be calculated as follows using the lag-one and lag-zero autocorrelation values:

$$\hat{b} = \sqrt{1 - \frac{|R_s(1)|}{|R_s(0)|}}. \quad (3)$$

4) Flow Speckle Speed: Another potentially useful information for the detection of aliasing at a given CFI pixel position is the motion of speckle patterns at that pixel. From a signal processing perspective, flow speckle maps can be

extracted from the log-compressed magnitudes of individual clutter-filtered slow-time ensembles. An optical flow algorithm can then be applied to these flow speckle maps to determine the motion vectors at different pixels. Subsequently, the flow speckle speed at each pixel can be determined as the magnitude of the corresponding motion vector. In this work, the Lucas–Kanade method [28] was used as the optical flow algorithm.

5) Flow Speckle Angle: Based on the motion vectors derived from optical flow analysis, directional information about inter-frame flow speckle motion can be obtained by computing the angle of each motion vector. This information served as a complementary data feature for aliasing detection.

C. Candidate Combinations for Training Features

Four combinations of training features were investigated for aliasing identification in CFI. In all training combinations, the Doppler frequency and the Doppler power were included because they were, respectively, the source of CFI aliasing and a direct indication of the presence of flow at a CFI pixel position (which may be aliased). Doppler bandwidth and flow speckle motion characteristics were included in some training combinations to test their supplementary value to the training of CNNs for aliasing detection. Based on this arrangement, the tested training combinations are listed as follows. In each case, one frame of training sample consisted of multiple data feature channels.

1) Doppler Frequency + Doppler Power: This combination was the basic case for CNN training.

2) Doppler Frequency + Doppler Power + Doppler Bandwidth: This combination was used to test if the inclusion of Doppler bandwidth information in the CNN training process could improve the performance of aliased pixel identification.

3) Doppler Frequency + Doppler Power + Flow Speckle Motion: In this combination, the benefit of flow speckle

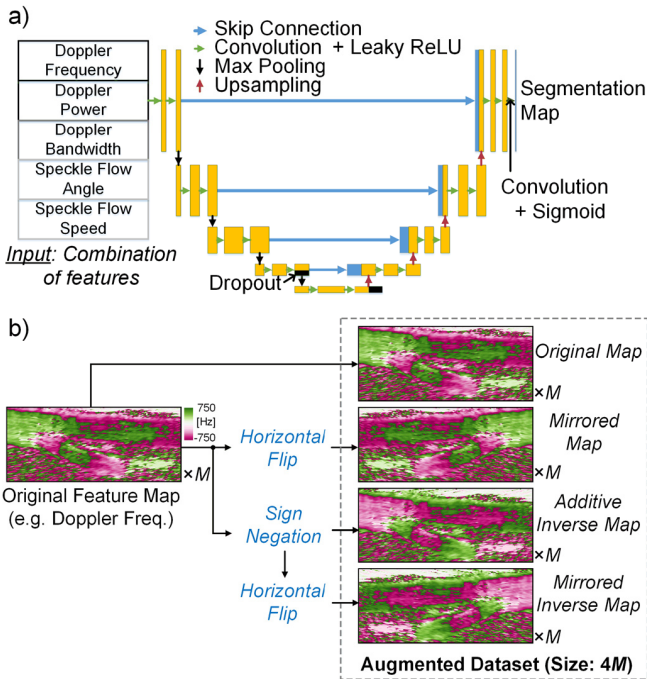


Fig. 3. Design and implementation of CNN for CFI aliasing detection. (a) Its architecture is based on a U-net with minor modifications, including leaky ReLUs, two dropout layers (denoted in black), and top-layer convolutional kernels whose number equaled to the number of training features. (b) CNN training was done using augmented data sets that comprised M original feature frames (e.g., the Doppler frequency maps) and their derived versions based on axial flipping, sign negation, and axial flipping with sign negation.

motion information in aliasing segmentation was investigated. Flow speckle motion was rendered as two additional feature data channels (speed and angle). Thus, in total, including Doppler frequency and Doppler power, each training sample consisted of four data feature channels.

4) *Doppler Frequency + Doppler Power + Doppler Bandwidth + Flow Speckle Motion*: This combination integrated all data features. In principle, it is expected to give the best CNN training performance for aliasing detection.

D. CNN Architecture

The neural network architecture used in this work was based on the U-net, which is a specific implementation of an encoder–decoder CNN [29]. This architecture was used because of its known effectiveness in performing image segmentation at a fine resolution [25]. It expands beyond the CNN architecture devised preliminarily by our group to address single-aliasing cases in CFI of flow phantoms [26]. As shown in Fig. 3(a), the CNN consists of an encoder part and a decoder part, each with 13 layers that are divided into five scales. Connecting the different scales are skip connections, where the output of an encoding layer is connected to a decoding layer of the same scale. The effective reception field of the encoder was 162×162 (pixels). The use of these network architecture parameters was empirically based on in-house pilot trials, and they were deemed to provide sufficient neighborhood information

to discern aliased CFI pixels. Note that the use of multiscale information is important in this CNN design because CFI aliasing can occur at varying regional sizes, from local to global discontinuities. Also, the use of skip connections is critical to improve both the training of deep networks and the segmentation resolution [25]. These connections can facilitate the training of CNNs that can track the often irregular and sharp boundaries of aliased regions in the CFI image view.

Since the CNNs used in this work were expected to process multiple channels of data features for each input frame, the first layer in the U-net architecture was modified from the original formulation [29] to include more convolutional kernels that equaled to the number of data feature channels in each input frame. In addition, leaky rectified linear units (ReLU) were used, and the leak parameter was set to 0.3. This CNN design choice was made to improve learning and to reduce the occurrence of “dying ReLU” cases [30]. Moreover, two 50% dropout layers were added [denoted in black in Fig. 3(a)] to improve the generalizability of the model. The size and number of filters were left as they were in the original U-net design [29].

E. Dealiasing and Image Regularization

Correction of aliasing errors was performed using an in-house adaptive phase unwrapping algorithm that is inspired by the literature [18]. In brief, it works by assuming that the segmented pixels were clustered in connected islands. As illustrated in Fig. 4(a), for each connected island, the internal and external boundary’s normalized CFI pixel values were extracted, and their median was evaluated. The difference between the internal and external boundary medians was then rounded to yield potential outcomes of -1 , 0 , or $+1$. In turn, this rounded difference outcome served to determine whether a negative or positive full-cycle phase should be subtracted from the CFI pixels of that aliased island to achieve phase unwrapping (or to not perform phase unwrapping if the rounded difference was 0).

In our dealiasing procedure, phase unwrapping was applied twice, as shown in Fig. 4(b). First, based on the segmentation results from CNN #1, phase unwrapping was applied once to the CFI pixel values of identified aliasing regions [i.e., either adding or subtracting the full-cycle phase based on the algorithm in Fig. 4(a)]. The output of this step was then fed through the same algorithm for a second time, wherein the segmentation results from CNN #2 were used to perform another round of phase unwrapping on double-aliasing cases. After these two rounds of phase unwrapping, the normalized Doppler frequency range effectively extended from $[-0.5, +0.5]$ to $[-2.5, +2.5]$.

At some pixel positions, aliasing may corrupt the pixels beyond utility. Indeed, our in-house spectral analysis showed significant folding due to aliasing and the normalized bandwidth approached unity in those pixels. To circumvent this issue, all pixels with a normalized Doppler bandwidth exceeding 0.9 were sifted from the resulting CFIs. In replacement, those sifted pixels were filled with a posthoc inpainting algorithm that consisted of averaging the nearest eight pixels

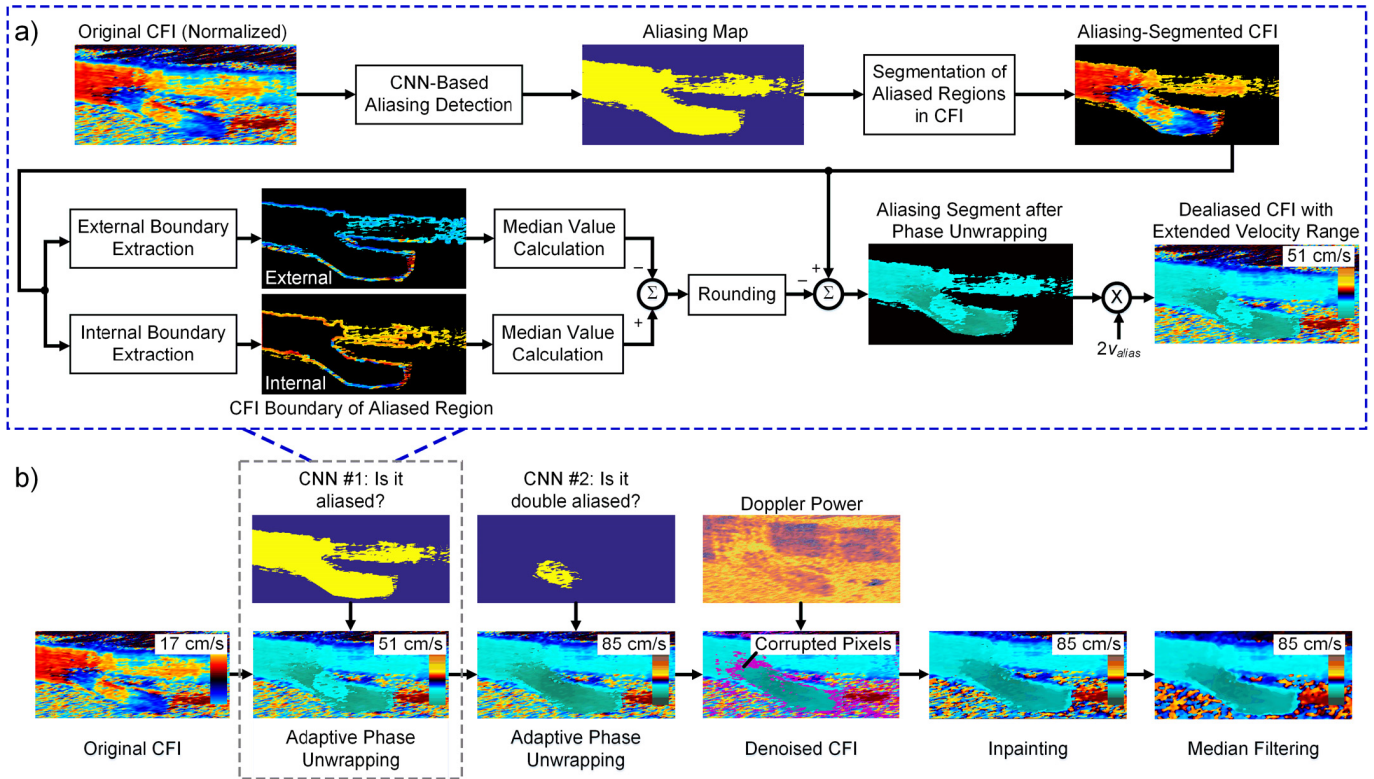


Fig. 4. Dealiasing based on CNN inference output. (a) Original normalized CFI is the first phase unwrapped once using the segmentation from CNN #1. External and internal boundaries of aliased CFI islands were extracted to determine the signage of full-cycle phase subtraction during phase unwrapping. $2v_{alias}$ denotes the original CFI dynamic range. (b) Stepwise illustration of the entire dealiasing algorithm. Phase unwrapping is performed for a second time using CNN #2 to resolve double-aliasing cases. Denoising, inpainting, and median filtering were then applied to regularize the dealiasing CFI values.

[fourth and fifth stages of Fig. 4(b)]. Finally, a 2-D median filter with a 5×5 kernel was applied to eliminate spurious values in the resulting CFI [last stage in Fig. 4(b)]. Note that the size of this median filter kernel was chosen empirically based on in-house testing to adequately remove spurious CFI values without distorting the flow profile.

III. EXPERIMENTAL METHODS

A. Data Collection

To facilitate performance investigation on the CNN-based dealiasing framework, *in vivo* data sets were acquired from ultrasound long-axis acquisitions of the femoral bifurcation, which was chosen for its non-trivial geometry and triphasic flow characteristics with large variations in flow velocity over a cardiac cycle [31]. Femoral CFI is generally susceptible to aliasing in the deep femoral artery branch, whose sloped vessel geometry naturally gives rise to smaller beam-to-flow angles that favor the generation of higher Doppler frequencies according to the Doppler equation. The femoral bifurcation from five healthy volunteers was imaged (with their written consent). To increase the variability of the data, the femoral bifurcation from each participant was also subjected to varying degrees of downstream pressure using a cuff set between 0 and 100 mmHg at increments of 20 mmHg. The data were collected as a part of a femoral bifurcation hemodynamics study protocol as approved by the human research ethics committee at the University of Waterloo. Each data acquisition trial was

performed over an entire cardiac cycle, so it included systolic and diastolic flow as well as flow reversal and recirculation.

Data acquisition was performed using an open-platform ultrasound research scanner (US4US; Warsaw, Poland) that was equipped with a linear array transducer (SL1543; Esaote, Genoa, Italy). The scanner was configured to perform plane-wave data acquisition, similar to what was described elsewhere [32]. Note that, instead of conducting conventional scanline-based imaging, plane wave data acquisition was performed in this work because of two reasons related to its high-frame-rate imaging capability. First, it allows for time-resolved tracking of femoral flow dynamics with significant spatiotemporal variations over different phases of a cardiac cycle. Second, it benefits the efficacy of our deep learning framework by providing a diverse range of training data input that spans time instants at both flow systole and diastole as well as ones with antegrade and retrograde flow. Accordingly, raw channel-domain ultrasound data sets of plane wave data acquisition were collected for offline processing. Table I summarized the imaging parameters used in this investigation. Note that a -10° steering angle was applied during each plane wave pulsing event. Also, the PRF was set to 1500 Hz, in line with what is used in clinical femoral CFI [31]. The use of such a low PRF was necessary to consistently track slow flow emerging during the flow transition phases of the cardiac cycle, thereby reducing color dropouts in the CFI cine loops. Both single- and double-aliasing artifacts were observed in the resulting CFI frames.

TABLE I
IMAGING PARAMETERS USED IN DATA COLLECTION

Parameter	Value
Imaging Platform	
Number of Tx/Rx channels	192
Array pitch	0.245 mm
Pre-beamformed data sampling rate	25 MHz
Pre-beamformed data resolution	12 bits
Data Acquisition	
Imaging frequency	5 MHz
Tx pulse duration (number of pulses)	3
Transmit steering angle	-10°
Pulse repetition frequency	1500 Hz
Data acquisition duration	3 s
Beamforming	
Pre-beamformed data filter passband	3-7 MHz
Filter design method	Equiripple (30 th Order)
Receive F-number	1.0
Receive steering angle	-10°
Pixel spacing (axial and lateral)	0.1 mm
Image dimension (number of pixels)	400 (axial) × 368 (lateral)
Image dimension (mm)	40.0 × 36.8

B. Signal Processing

The raw data sets collected from the scanner were processed in MATLAB (version 2016a; MathWorks, Natick, MA, USA) to generate the five training features described in Section II-B. The processing platform was a computer server (SYS-4028-TRT; Super Micro, San Jose, CA, USA) that was equipped with a Xeon E5-2620 central processing unit (Intel, Santa Clara, CA, USA) and an RTX-2080 graphical processing unit (GPU) (Nvidia, Santa Clara). Using MATLAB, beamforming was performed on this platform via a GPU-based delay-and-sum algorithm [33], with the Gaussian apodization window and dynamic receive focusing. The key processing parameters are listed in Table I. Note that the receive aperture size (i.e., number of channels used to form each pixel) was automatically adjusted within GPU beamformer to consistently achieve an F-number of 1.0 for all pixel positions, thus yielding a lateral beamwidth of 0.68 mm (full-width at half-maximum value; derived from in-house field simulations). The receive aperture's lateral position was automatically centered about the corresponding pixel in all instances. Also, a steering angle of -10° was applied during this beamforming process to avoid instances of a 90° beam-to-flow angle at different pixel positions.

From the beamformed data frames generated, slow-time clutter filtering was performed at each pixel position using an equiripple infinite impulse response filter with a cutoff of 0.1 normalized frequency (i.e., 150 Hz). Subsequently, the Doppler frequency, the Doppler power, and the Doppler bandwidth were computed at each pixel position using an ensemble size of 48 and the formulas in Section II-B. Also, optical flow analysis (using the Lucas-Kanade algorithm) was performed on the log-compressed, clutter-filtered data frames to determine the flow speckle speed and the flow speckle angle at each pixel position. For this analysis, data for flow speckle speed and angle were averaged over 32 frames to reduce noise.

For CNN training, the computed values for all these features were normalized with respect to the largest magnitude value of each map frame.

C. Data Organization for CNN Training

In total, eight acquisitions were performed. Among all data frames, 284 CFI frame samples were generated for CNN training. The data feature frames used for the training of CNN #1 (for general identification of aliasing, including both single and double cases) were augmented to improve generalizability. Specifically, as illustrated in Fig. 3(b), the data feature frames were flipped about their depth axis to introduce flow conditions going in the opposite lateral direction; moreover, for the Doppler frequency frames and optical flow angle frames, their additive inverse forms were derived to change the assumed flow direction. In total, the augmentations resulted in a final training set of 1136 frames (i.e., fourfold of the 284 original CFI frame samples). It is worth noting that the number of pixels affected by double aliasing constituted only a small portion of the entire data set. As such, for CNN #2 (intended to solely identify double aliasing), another training set was produced by excluding all frames without double aliasing. In turn, 476 frame samples were used to train CNN #2.

For each frame of training data, aliased regions were manually segmented to provide CNN with information on where aliasing appeared in the image view. This manual segmentation task was performed using built-in MATLAB functions. As shown in Fig. 5(a), it first involved, by inspection, manual demarcation of the aliased zone as a polygon based on the criterion that aliased CFI pixels were manifested as anomalous color hue changes (i.e., a sudden change from red to blue, or vice versa). After that, an aliasing reference map was formed by finding, within the demarcated polygon, the CFI pixels with Doppler frequency signage that was opposite of that for the expected flow direction. For aliased frames with both single aliasing and double aliasing, manual segmentation was based on a multistep process. As illustrated in Fig. 5(b), it first identified a primary zone and searched for aliased CFI pixels in the same way as the simpler case shown in Fig. 5(a). Subsequently, the aliasing reference map was refined by performing another round of manual demarcation that delineated the boundaries of single-aliasing regions with CFI pixels whose color was the same as that for flow. This supplementary demarcation was achieved based on manual identification of CFI map islands that were surrounded by single-aliased pixels with anomalous color hue change. All pixels within this supplementary zone were then labeled as aliased in the final aliasing reference map. Note that, following a similar manual segmentation procedure, double-aliasing zones were separately identified on each CFI frame based on the principle that each of these zones would be engulfed within a single-aliased region that shared the same CFI color as that for flow.

D. Training Implementation

To facilitate CNN training and inference, Python (version 3.6.7) scripts were written for data fetching

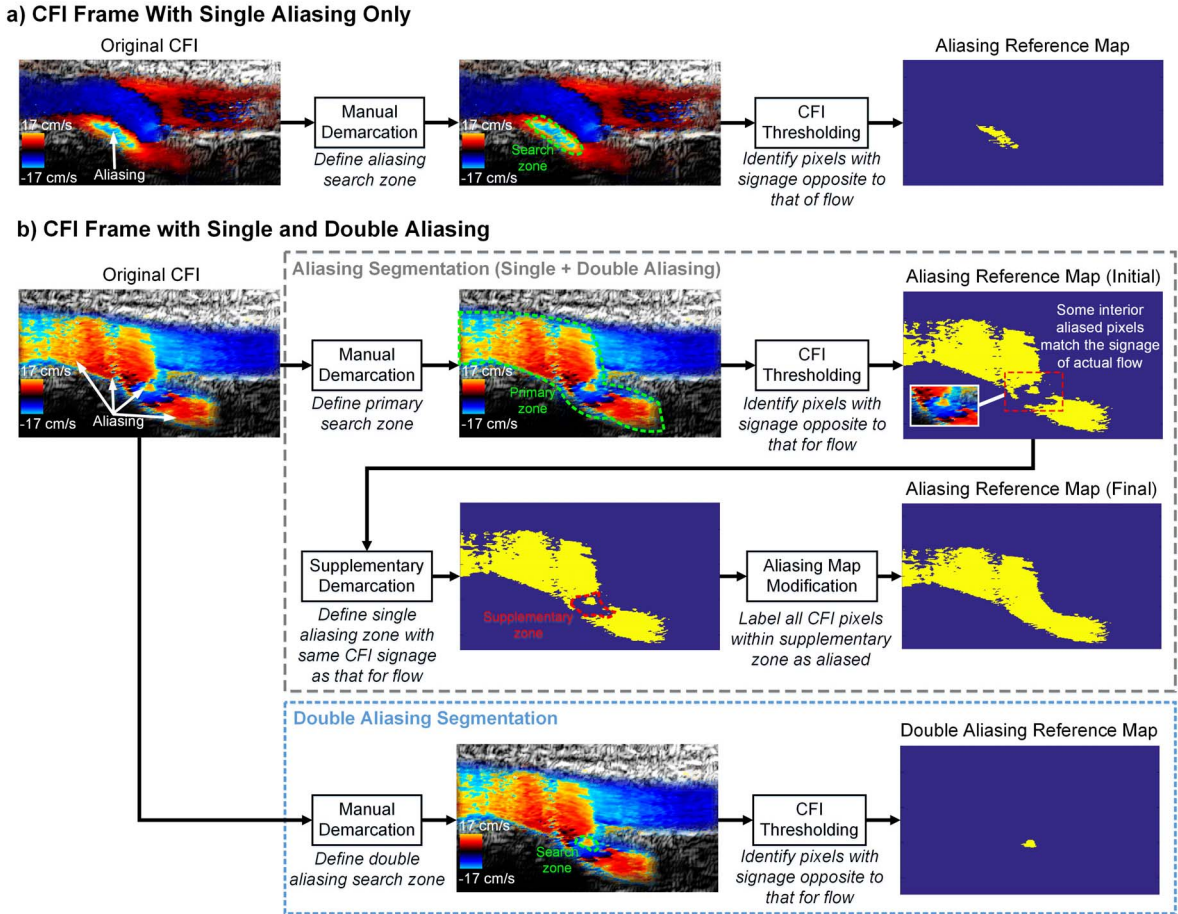


Fig. 5. Illustration of the manual segmentation procedure, as applied to CFI frames with (a) single aliasing only and (b) single aliasing and double aliasing. For the latter, the procedure was separately performed to obtain the aliasing reference map (covering both single aliasing and double aliasing) and the double-aliasing reference map.

and for the execution of CNN-related operations on the computing server's RTX-2080 GPU. These scripts included calls to the Keras application programming interface (API) (version 2.1.6) that served to: 1) define the U-net CNN architecture parameters and 2) invoke CNN computation operations on the RTX-2080 GPU via implicit calls to the TensorFlow-GPU (version 1.12) software back end. Each CNN was trained by optimizing the binary cross-entropy loss between prediction and the reference outcome derived from manual segmentation. Such optimization was achieved using Adam optimizer [34] with a learning rate of 10^{-4} . To prevent overfitting, an early stopping mechanism was implemented such that the training was terminated when the loss on the validation set did not improve for 5 epochs. Moreover, only the model with the lowest validation loss was saved from each training procedure. Memory constraints in the GPU hardware (with only 8 GB of random access memory) necessitated a batch size of 1. To account for the variability of initialization and data sampling, seven models (i.e., seven CNN training trials) with different random starting conditions were trained for each training feature combination, and their performance distribution was analyzed.

E. Testing and Segmentation Evaluation

With the trained CNNs, inferences on aliasing detection were made on 100 test frames that were acquired on a different subject. Phase unwrapping was performed using the algorithm described in Section II-E to recover the expected flow profile. The prediction results were compared against references derived from manual segmentation of aliased regions (realized using the same procedure presented in Section III-C). The efficacy of a CNN in identifying aliased pixel positions was evaluated using precision, recall, and intersection-over-union (IoU) metrics that are, respectively, defined as follows:

$$\text{Precision} = \frac{|y \cap \hat{y}|}{|\hat{y}|} \quad (4)$$

$$\text{Recall} = \frac{|y \cap \hat{y}|}{|y|} \quad (5)$$

$$\text{IoU} = \frac{|y \cap \hat{y}|}{|y \cup \hat{y}|} \quad (6)$$

where $|\cdot|$ denotes the size of the set, y is the reference segmentation map, as obtained from manual segmentation, and \hat{y} is the predicted segmentation for aliasing.

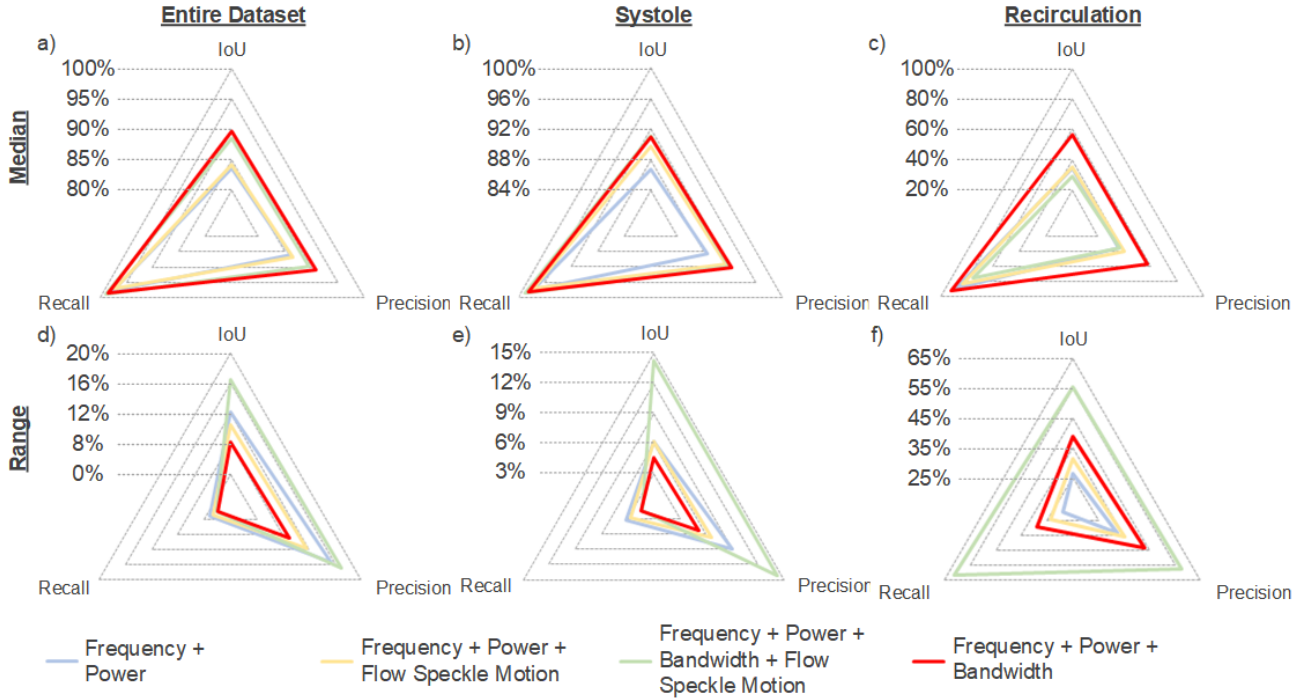


Fig. 6. Radar plots of recall, precision, and IoU for four feature combinations in training aliasing-detection CNNs. Over seven CNN training and inference trials, the median values are shown in different test cases. (a) Entire data set for femoral CFI. (b) CFI frames taken during systole. (c) CFI frames taken during postsystolic recirculation. (d)–(f) each metric’s range (i.e., maximum minus minimum) in the seven trials.

An adjunct CNN training and inference experiment was performed to gain cursory insight into the effects of reduced training data size on CNN’s aliasing detection performance. This adjunct experiment was conducted using a subset of 159 CFI frames formed from five of the eight human volunteer acquisitions. It made use of the same training data augmentation strategy and CNN implementation specifics as described in Sections III-C and III-D. The corresponding precision, recall, and IoU were derived for result analysis.

F. Dealiasing Performance Evaluation

The dealiased CFI frames obtained from the CNN-based framework were compared with the ones obtained from manual dealiasing, which involved manual segmentation of aliased pixel positions (as explained in Section III-C) and the use of the same dealiasing algorithm presented in Section II-E. Their difference was quantified using the root-mean-squared difference (RMSD) metric, which is defined as

$$\text{RMSD} = \sqrt{\frac{1}{M} \sum_{i=1}^M [x_{i(\text{CNN})} - x_{i(\text{manual})}]^2} \quad (7)$$

where M is the number of pixels being evaluated, while $x_{i(\text{CNN})}$ and $x_{i(\text{manual})}$ are respective the i th pixel value in the CNN-based dealiased CFI and in the manually dealiased CFI. The results were normalized with respect to the postcorrection, extended Doppler frequency limit (i.e., $5f_{\text{max}}$).

IV. RESULTS

A. CNNs Trained With Frequency, Power, and Bandwidth Features Yielded the Best Aliasing Detection Performance

For aliasing-detection CNNs, all candidate combinations of training features being tested (as presented in Section II-C) had converged in training, and they yielded CNNs with varying degrees of success in identifying aliasing (whether it is single aliasing or double aliasing) at different pixel positions. Fig. 6 summarizes the aliasing segmentation performance for the CNN of each training feature combination by plotting the median and range (i.e., maximum minus minimum) of its precision, recall, and IoU derived from seven CNN training trials. Results are shown for different test cases: over the entire test set (left column), for CFI frames taken during systole (middle column), and for CFI frames acquired in the presence of flow recirculation (right column).

As shown in Fig. 6, the CNN exhibited the best aliasing detection performance when it was trained using the features of Doppler frequency, Doppler power, and Doppler bandwidth (red line in the plots). This training feature combination yielded the highest median recall, precision, and IoU for the seven CNN training trials in all test cases. Indeed, for the global test case, the recall, precision, and IoU were, respectively, 98.5%, 90.5%, and 89.7%. In comparison, for an adjunct inference experiment conducted with a CNN trained using frequency, power, and bandwidth features derived from a reduced data set of 159 CFI training frame samples (versus 284 in the main experiment), the global test case had

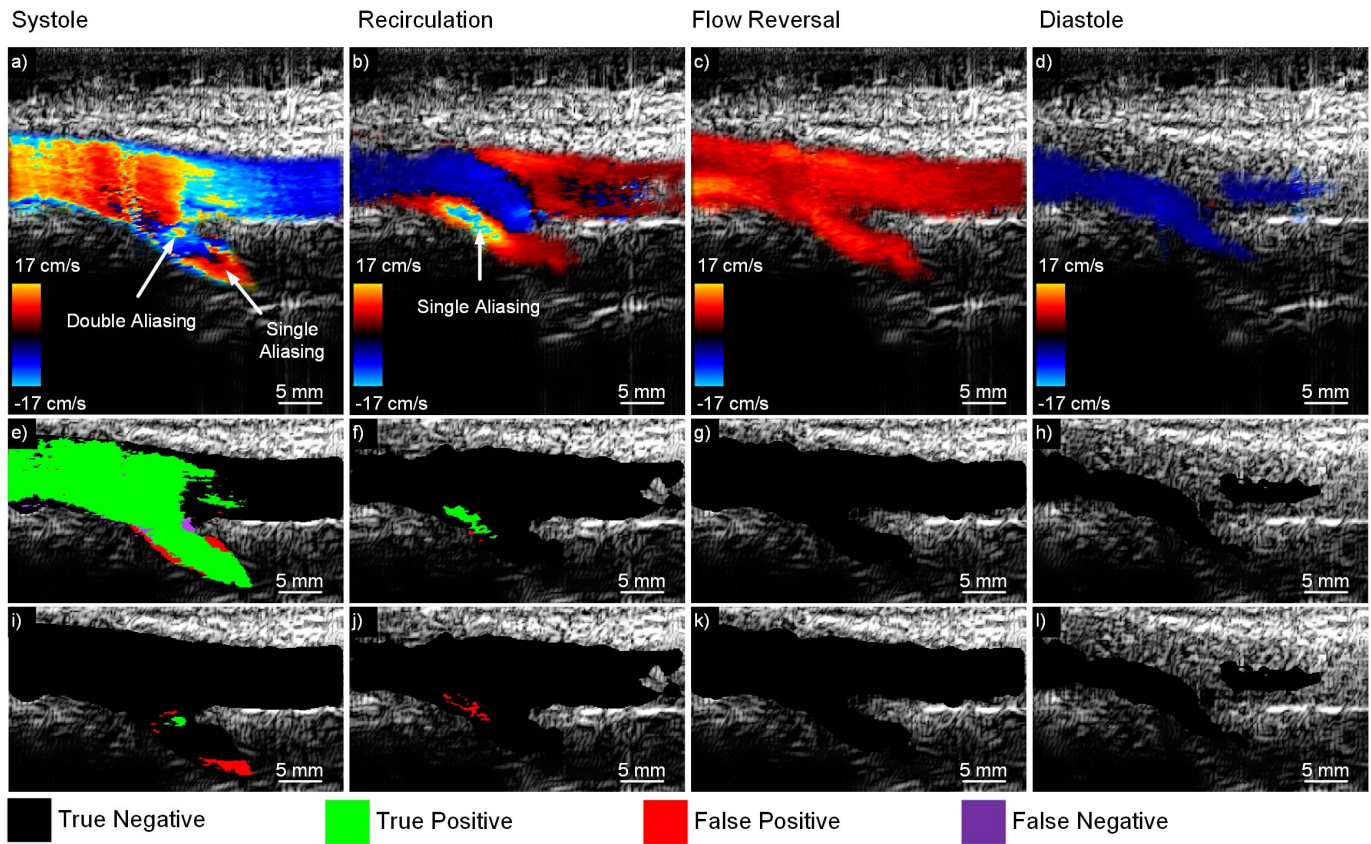


Fig. 7. Segmentation performance of the aliasing-detection CNNs. (a)–(d) Original CFI at different phases of the cardiac cycle. (e)–(h) Aliased regions (including both single aliasing and double aliasing) identified by CNN #1, with errors color-coded. (i)–(l) Double-aliased regions identified by CNN #2, with errors color-coded. All images are overlaid on top of the original B-mode images.

achieved a recall, precision, and IoU of 88.5%, 85.9%, and 88.2%, respectively (data not shown).

Another observation from Fig. 6 is that the CNN of the frequency–power–bandwidth training combination generally yielded the smallest range for the three metrics in the global test case and the systolic frameset test case. While this CNN yielded a mediocre median precision and IoU of just above 50% in the test case involving CFI frames with flow recirculation, it was still significantly higher than those for the CNN of other training combinations by at least 15%. It is worth noting that, for the CNN of the frequency–power–bandwidth training combination, the inference time required to generate one frame of aliasing segmentation result was found to be 44 ms when the inference procedure was executed on the RTX-2080 GPU.


B. Aliasing-Detection CNN Can Accurately Identify Most of the Aliased Pixels

Using the three-feature training combination involving frequency, power, and bandwidth, the trained CNN was found to be potent in correctly identifying the majority of aliased pixels in the image view over different phases of a cardiac cycle. Fig. 7 shows the corresponding results for four representative time points (systole, postdiastolic recirculation, flow reversal, and diastole). For the CFI frames shown on the first row of Fig. 7, the bottom two rows show maps of the detection performance for CNN #1 (for general aliasing identification,

including both single- and double-aliasing cases) and CNN #2 (for double-aliasing detection only). Four color-coded detection outcome regions are rendered in each map: true positive (green), true negative (black), false positive (red), and false negative (purple).

As can be observed from Fig. 7, CNN #1 exhibited a strong performance in correctly identifying aliased pixels throughout the cardiac cycle. Specifically, it was able to identify most of the aliased pixels in the systole frame and in the CFI frame with postsystolic circulation. There were a limited number of false-positive and false-negative pixels near the tissue-flow boundary. In the flow reversal and diastole CFI frames, this CNN yielded true negative detection results with no detection error. On the other hand, for CNN #2, whose role was to solely detect double-aliasing cases, it was able to correctly identify the double-aliasing zone in the systole CFI frame [green zone in Fig. 7(h)]. Nevertheless, it also yielded some false-positive instances in the form of scattered islands in certain CFI frames [red zones in Fig. 7(h) and (i)].

C. Visualization of Dealiased CFI Frames After Adaptive Phase Unwrapping

Based on the CNN-identified aliasing regions, adaptive phase unwrapping was found to be capable of resolving single- and double-aliasing artifacts in the CFI frames taken during systole and in the presence of recirculation. As an illustration,  Movie 1 shows a cine loop (playback rate: 30 frames/s)

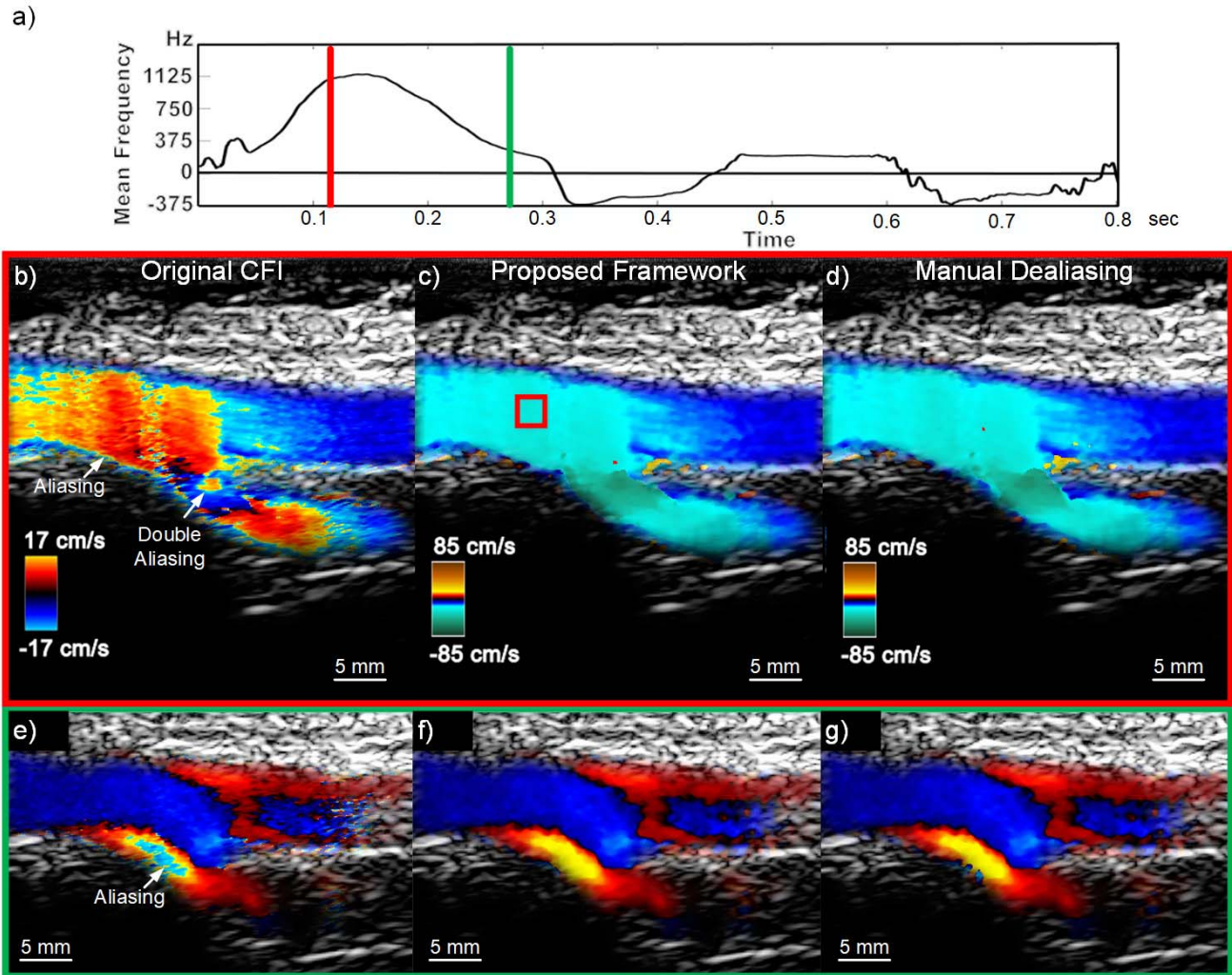


Fig. 8. CFI visualization of femoral bifurcation before and after dealiasing. In (a), the time plot of spatially averaged Doppler frequency is shown for the red box shown in (c); two time points of interest are indicated: systole (red line) and postsystolic recirculation (green line). For systole, three CFI frames are shown. (b) Original without dealiasing. (c) After dealiasing using the proposed framework. (d) After manual dealiasing. (e)–(g) Corresponding results for postsystolic recirculation.

of dealiased CFI over an entire triphasic cardiac cycle in the femoral bifurcation. Shown in this movie is a side-by-side comparison between the original CFI (left column), the dealiased CFI (middle column), and the CNN-derived aliasing segmentation map (right column). Representative temporal snapshots of dealiased CFI are shown in Fig. 8, specifically for frames taken during systole (red box), postsystolic recirculation (green box), flow reversal (blue box), and diastole (yellow box). Note that the velocity scale bars in Movie 1 and Fig. 8, as derived from the Doppler equation assuming 0° beam-to-flow angle, are not the same for the original and the dealiased CFI because of their difference in the Doppler frequency range (see Section II-E). Also, for reference, a time plot of postcorrection mean Doppler frequency (spatial-averaged over the red box within the dealiased CFI) is shown in the top row of Movie 1 and Fig. 8.

Three major observations should be noted in the dealiased CFI results. First, after resolving the aliasing artifacts, antero-grade flow during systole can be consistently visualized in the dealiased CFI (red box; Fig. 8). Second, during postsystolic

recirculation, the dealiased CFI yielded a more consistent depiction of the flow recirculation zone compared with the unaliased CFI (green box; Fig. 8). Third, when comparing with the segmentation results in Fig. 7, the extraneous pixels that were misidentified as double aliasing did not significantly affect the visualization performance of the dealiased CFI because connected bodies of misidentified pixels were not phase unwrapped as they did not exhibit a significant difference with respect to their neighborhood.

For the dealiased CFI frames, their RMSD relative to the reference based on manual segmentation and dealiasing is shown in Table II. In all test cases (global, systole, and recirculation), NRMSD values were under 2.51%, indicating that the CNN-based dealiasing approach yielded similar CFI quality as the manual approach.

V. DISCUSSION

A. Summary of Contributions

In recent years, the application potential of deep learning in medical imaging is serendipitously becoming established

TABLE II
RMSD BETWEEN THE CNN-BASED DEALIASED CFI
AND THE MANUALLY DEALIASED CFI

Test Case Type	RMSD (%)
Global	1.61
Systole	2.51
Recirculation	1.16

due to the concurrent advances in high-throughput computing hardware such as the GPU. Harnessing such emerging potency, this work represents the first attempt to address the aliasing problem in ultrasound CFI scenarios *in vivo* using a deep learning approach. In particular, we have devised and trained CNNs to identify and segment aliasing artifacts in CFI using multiple data features derived from different steps of the CFI data processing pipeline (see Fig. 2). The CNNs were trained based on a U-net architecture (see Fig. 3), and inferences drawn from the trained CNNs were used to correct for aliasing errors (both single- and double-aliasing cases) through an adaptive phase unwrapping strategy (see Fig. 4). Our *in vivo* femoral bifurcation experiments showed that the new dealiasing framework was able to detect aliased CFI pixels (see Fig. 7) and, in turn, resolve them to generate unaliased CFIs with the Doppler frequency dynamic range that was five times wider than the conventional range (🎬 Movie 1 and Fig. 8).

Compared with existing CFI dealiasing methods [17], [18], our CNN-based segmentation approach made no assumptions on the size of aliasing region(s) in the image view and incorporated multiple CFI data features to achieve more consistent aliasing detection performance. In doing so, our framework was able to identify single- and double-aliasing zones even in CFI frames taken where the majority of the flow region was aliased (see Fig. 7, top row). In addition, our framework did not falsely identify CFI regions with arbitrary discontinuities as aliased pixels (such as those emerging from recirculation zones). As well, it was able to extrapolate aliasing segmentation to regions where its boundaries were ill-defined.

It is worth reiterating that aliasing occurs in CFI whenever the PRF is lower than the Nyquist limit such that the actual Doppler frequency is greater than the maximum unaliased frequency. On this issue, our CNN-based dealiasing framework has served well to relax the Nyquist constraint in CFI by identifying and correcting CFI pixels with the aliased Doppler frequency estimates such that they would not disrupt CFI's flow map appearance. In achieving so, CFI can ascertain itself as a flow mapping modality that is resilient against aliasing artifacts even when a relatively low PRF is used. This notion has been demonstrated in our femoral imaging experiments. Bolstering CFI's resilience against aliasing would also be of practical significance to other flow mapping scenarios *in vivo* (to be elaborated in Section V-C).

B. Insights on CNN Training for Aliasing Detection

As a part of this investigation, different combinations of data features were used to train CNNs for aliasing detection.

It was found that the combined use of Doppler frequency, Doppler power, and Doppler bandwidth led to the best aliasing detection performance as quantified from the metrics of recall, precision, and IoU (see Fig. 6). Note that as substantiated by the strong performance metrics for this training feature combination, the size of training data sets used for CNN development can generally be regarded as adequate in our experiments. Even if CNN was trained with 56% of the original data set size, the resulting aliasing segmentation performance was only reduced slightly, as mentioned in Section IV-A.

Doppler frequency and power were obvious to include as training features given their respective roles as the origin of CFI aliasing and the primary flow indicator. In contrast, Doppler bandwidth's utility in aliasing segmentation can be rationalized by noting that the Doppler spectral contents exceeding the Nyquist limit were unpredictably rendered as aliased spectral contents in the sampled spectrum, thus adding variability to the estimated Doppler bandwidth. In turn, these spurious bandwidth estimates manifested themselves as spatial outliers over a 2-D frame of bandwidth estimates, so they served well as complementary training input for the CNNs.

Flow speckle motion, as derived from optical flow analysis, was considered as a candidate data feature for CNN training. Nonetheless, it did not seem to improve aliasing detection. The reason is likely because speckle tracking is prone to be inconsistent in scenarios with low signal-to-noise ratios as was the case in flow estimation [35]. If flow speckle motion is to become a practically useful training feature for CNN-based aliasing detection, more advanced speckle tracking algorithms probably need to be implemented [36].

C. Applications of Interest

In practice, there are at least three scenarios *in vivo* where aliasing is inevitably prone to occur. The first scenario is when a relatively low PRF is used to track slow flow in a pulsatile flow cycle with the fast systolic flow. For instance, we used a PRF of 1500 Hz for femoral bifurcation flow imaging. The use of this relatively low PRF value, which was in accordance with that used clinically in femoral CFI [31], was necessary to capture slow but dynamic flow patterns that occurred during the flow phase transitions of the artery's triphasic pulsatile flow cycle. However, as a result of using this low PRF value, aliasing unavoidably emerged during systole with fast flow velocities. After performing dealiasing with our algorithm, the resulting CFI flow visualization became more visually intuitive, as rendered in 🎬 Movie 1 and Fig. 8.

The second applicable scenario arises when a relatively low PRF is needed to monitor fast flow dynamics away from the surface. As known in pulse-echo imaging, the maximum PRF that can be used is inversely proportional to the maximum intended imaging depth (since $\text{PRF}_{\max} = c_o/2z_{\max}$). Because the choice of PRF is limited by the depth resolvability constraint, aliasing would be inevitable when the flow is relatively fast. Accordingly, an effective dealiasing algorithm is needed to resolve aliasing artifacts originating from pixels with fast flow. Practical examples of this imaging scenario include: 1) intraventricular flow imaging [37], and

2) transperineum urinary flow imaging [38]. In these cases, flow speeds can be well above 2 m/s, and the beam-to-flow angles may be small; in turn, the actual Doppler frequency may be relatively high. Nevertheless, the imaging depth can be up to 20 cm (for cardiac imaging) and 8 cm (for peritoneal urinary flow imaging), thus precluding the use of a high PRF, such as 10000 Hz.

The third application scenario of interest is when relatively fast flow speeds emerge in the CFI image view. A prime example of this application scenario is the high-speed flow jet that arises at a carotid artery stenosis site. These flow jets can readily yield a peak systolic velocity of over 3 m/s for stenotic sites whose narrowing level is 70% or higher [39]. In such a peripheral flow mapping scenario, CFI may be performed with a relatively high PRF of 10000 Hz. However, aliasing is still prone to occur since, according to the Doppler equation, the actual Doppler frequency tends to be high (and greater than the maximum unaliased frequency) due to the fast flow speed.

Aside from CFI applications, the CNN-based dealiasing algorithm may be applied to vector Doppler estimation. Aliasing is an inherent concern in vector Doppler estimation because the use of multiple transmit angles necessitates the use of lower PRF values for the Doppler estimation at each angle [40]. To tackle the aliasing problem in vector Doppler, different CNNs can be trained for each angle to remove aliasing from that angle. Note that the segmentation maps obtained here may be used with more advanced aliasing resistant algorithms [41] suited for vector flow imaging to minimize their errors.

D. Limitations of Investigation

A few caveats should be acknowledged about the current body of work. First, when assessing the aliasing detection performance of our CNN-based framework, we have primarily made reference to manually identified aliased CFI regions. It would be beneficial in the future to more comprehensively validate the efficacy of our proposed algorithm by comparing its dealiased CFI maps with flow profiles obtained from another intraluminal flow measurement technique such as magnetic resonance angiography.

Another limitation to be noted is that since the application focus of this work was exclusively on femoral CFI, we have yet to evaluate the efficacy of CNN-based dealiasing in other CFI scenarios, such as the ones mentioned in Section V-C. To generalize our dealiasing algorithm in other CFI scenarios, the CNNs should be retrained to include sample input from these imaging scenarios. Along this line of investigation, it would also be worthwhile to verify the robustness of the new dealiasing framework for different training data set sizes and when applying it to CFI data acquired using different imaging parameters.

VI. CONCLUSION

Aliasing has been a long-standing nuisance in CFI. With the use of our CNN-based dealiasing algorithm, CFI pixels suffering from single aliasing or double aliasing were identified,

and they were resolved through adaptive phase unwrapping to effectively extend the Doppler dynamic range by fivefold. In doing so, CFI flow visualization quality was significantly improved. Through creating properly trained CNNs for aliasing detection, the proposed framework is expected to help disentangle aliased-induced color mosaics in CFI frames. In turn, it can potentially improve CFI's utility in clinical vascular diagnostics, especially in cases with tortuous vessels with significant temporal variations in flow profile.

REFERENCES

- [1] C. R. B. Merritt, "Doppler color flow imaging," *J. Clin. Ultrasound*, vol. 15, no. 9, pp. 591–597, Nov. 1987.
- [2] A. A. Oglat, M. Z. Matjafri, N. Suardi, M. A. Oqlat, M. A. Abdelrahman, and A. A. Oqlat, "A review of medical Doppler ultrasonography of blood flow in general and especially in common carotid artery," *J. Med. Ultrasound*, vol. 26, no. 1, pp. 3–13, Jan. 2018.
- [3] M. Thiriet, M. Delfour, and A. Garon, "Vascular stenosis: An introduction," in *PanVascular Medicine*, P. Lanzer, Ed. Berlin, Germany: Springer, 2015, pp. 781–868.
- [4] W. D. Foley and S. J. Erickson, "Color Doppler flow imaging," *Amer. J. Roentgenol.*, vol. 156, no. 1, pp. 3–13, Jan. 1991.
- [5] L. Terslev, A. P. Diamantopoulos, U. M. Dohn, W. A. Schmidt, and S. Torp-Pedersen, "Settings and artefacts relevant for Doppler ultrasound in large vessel vasculitis," *Arthritis Res. Therapy*, vol. 19, no. 1, pp. 167–177, Dec. 2017.
- [6] A. Goddi *et al.*, "High-frame rate vector flow imaging of the carotid bifurcation in healthy adults: Comparison with color Doppler imaging," *J. Ultrasound Med.*, vol. 37, no. 9, pp. 2263–2275, Sep. 2018.
- [7] J. A. Jensen, S. I. Nikolov, A. C. H. Yu, and D. Garcia, "Ultrasound vector flow imaging—Part II: Parallel systems," *IEEE Trans. Ultrason., Ferroelectr., Freq. Control*, vol. 63, no. 11, pp. 1722–1732, Nov. 2016.
- [8] J. A. Jensen, S. I. Nikolov, A. C. H. Yu, and D. Garcia, "Ultrasound vector flow imaging—Part I: Sequential systems," *IEEE Trans. Ultrason., Ferroelectr., Freq. Control*, vol. 63, no. 11, pp. 1704–1721, Nov. 2016.
- [9] M. Cikes, L. Tong, G. R. Sutherland, and J. D'Hooge, "Ultrafast cardiac ultrasound imaging: Technical principles, applications, and clinical benefits," *JACC Cardiovascular Imag.*, vol. 7, no. 8, pp. 812–823, Aug. 2014.
- [10] A. Goddi *et al.*, "High-frame rate vector flow imaging of the carotid bifurcation," *Insights into Imag.*, vol. 8, no. 3, pp. 319–328, Jun. 2017.
- [11] K. L. Hansen, H. Møller-Sørensen, J. Kjaergaard, M. B. Jensen, J. A. Jensen, and M. B. Nielsen, "Aortic valve stenosis increases helical flow and flow complexity: A study of intra-operative cardiac vector flow imaging," *Ultrasound Med. Biol.*, vol. 43, no. 8, pp. 1607–1617, Aug. 2017.
- [12] K. L. Hansen *et al.*, "Intra-operative vector flow imaging using ultrasound of the ascending aorta among 40 patients with normal, stenotic and replaced aortic valves," *Ultrasound Med. Biol.*, vol. 42, no. 10, pp. 2414–2422, Oct. 2016.
- [13] A. Swillens, P. Segers, and L. Lovstakken, "Two-dimensional flow imaging in the carotid bifurcation using a combined speckle tracking and phase-shift estimator: A study based on ultrasound simulations and *in vivo* analysis," *Ultrasound Med. Biol.*, vol. 36, no. 10, pp. 1722–1735, Oct. 2010.
- [14] B. Y. S. Yiu, S. S. M. Lai, and A. C. H. Yu, "Vector projectile imaging: Time-resolved dynamic visualization of complex flow patterns," *Ultrasound Med. Biol.*, vol. 40, no. 9, pp. 2295–2309, Sep. 2014.
- [15] X. Lai, H. Torp, and K. Kristoffersen, "An extended autocorrelation method for estimation of blood velocity," *IEEE Trans. Ultrason., Ferroelectr., Freq. Control*, vol. 44, no. 6, pp. 1332–1342, Nov. 1997.
- [16] D. Posada *et al.*, "Staggered multiple-PRF ultrafast color Doppler," *IEEE Trans. Med. Imag.*, vol. 35, no. 6, pp. 1510–1521, Jun. 2016.
- [17] A. Shahin, M. Ménard, and M. Eboueya, "Cooperation of fuzzy segmentation operators for correction aliasing phenomenon in 3D color Doppler imaging," *Artif. Intell. Med.*, vol. 19, no. 2, pp. 121–154, Jun. 2000.
- [18] S. Muth, S. Dort, I. A. Sebag, M.-J. Blais, and D. Garcia, "Unsupervised dealiasing and denoising of color-Doppler data," *Med. Image Anal.*, vol. 15, no. 4, pp. 577–588, Aug. 2011.

- [19] A. Garcia-Garcia, S. Orts-Escolano, S. Oprea, V. Villena-Martinez, and J. Garcia-Rodriguez, "A review on deep learning techniques applied to semantic segmentation," 2017, *arXiv:1704.06857*. [Online]. Available: <http://arxiv.org/abs/1704.06857>
- [20] J. Long, E. Shelhamer, and T. Darrell, "Fully convolutional networks for semantic segmentation," in *Proc. IEEE Conf. Comput. Vis. Pattern Recognit. (CVPR)*, Jun. 2015, pp. 3431–3440.
- [21] V. Badrinarayanan, A. Kendall, and R. Cipolla, "SegNet: A deep convolutional encoder-decoder architecture for image segmentation," *IEEE Trans. Pattern Anal. Mach. Intell.*, vol. 39, no. 12, pp. 2481–2495, Dec. 2017.
- [22] H. Dong, G. Yang, F. Liu, Y. Mo, and Y. Guo, "Automatic brain tumor detection and segmentation using U-Net based fully convolutional networks," in *Proc. Annu. Conf. Med. Image Understand. Anal.*, 2017, pp. 506–517.
- [23] M. H. Yap *et al.*, "Automated breast ultrasound lesions detection using convolutional neural networks," *IEEE J. Biomed. Health Inform.*, vol. 22, no. 4, pp. 1218–1226, Jul. 2018.
- [24] J. C. Ye and W. K. Sung, "Understanding geometry of encoder-decoder CNNs," 2019, *arXiv:1901.07647*. [Online]. Available: <http://arxiv.org/abs/1901.07647>
- [25] M. Drozdal, E. Vorontsov, G. Chartrand, S. Kadoury, and C. Pal, "The importance of skip connections in biomedical image segmentation," in *Proc. Deep Learn. Data Labeling Med. Appl.*, in Lecture Notes in Computer Science, 2016, pp. 179–187.
- [26] H. Nahas, T. Ishii, A. J. Y. Chee, B. Y. S. Yiu, and A. C. H. Yu, "Segmentation of aliasing artefacts in ultrasound color flow imaging using convolutional neural networks," in *Proc. Image Anal. Recognit.*, in Lecture Notes in Computer Science, vol. 11663, 2019, pp. 452–461.
- [27] C. Kasai, K. Namekawa, A. Koyano, and R. Omoto, "Real-time two-dimensional blood flow imaging using an autocorrelation technique," *IEEE Trans. Sonics Ultrason.*, vol. TSU-32, no. 3, pp. 458–464, May 1985.
- [28] S. Baker and I. Matthews, "Lucas-Kanade 20 years on: A unifying framework," *Int. J. Comput. Vis.*, vol. 56, no. 3, pp. 221–255, Feb. 2004.
- [29] O. Ronneberger, P. Fischer, and T. Brox, "U-Net: Convolutional networks for biomedical image segmentation," in *Proc. Med. Image Comput. Comput.-Assist. Intervent.*, 2015, pp. 234–241.
- [30] L. Lu, Y. Shin, Y. Su, and G. E. Karniadakis, "Dying ReLU and initialization: Theory and numerical examples," 2019, *arXiv:1903.06733*. [Online]. Available: <http://arxiv.org/abs/1903.06733>
- [31] J. Y. Hwang, "Doppler ultrasonography of the lower extremity arteries: Anatomy and scanning guidelines," *Ultrasonography*, vol. 36, no. 2, pp. 111–119, Apr. 2017.
- [32] B. Y. S. Yiu, M. Walczak, M. Lewandowski, and A. C. H. Yu, "Live ultrasound color-encoded speckle imaging platform for real-time complex flow visualization *in vivo*," *IEEE Trans. Ultrason., Ferroelectr., Freq. Control*, vol. 66, no. 4, pp. 656–668, Apr. 2019.
- [33] B. Y. S. Yiu, I. K. H. Tsang, and A. C. H. Yu, "GPU-based beamformer: Fast realization of plane wave compounding and synthetic aperture imaging," *IEEE Trans. Ultrason., Ferroelectr., Freq. Control*, vol. 58, no. 8, pp. 1698–1705, Aug. 2011.
- [34] D. P. Kingma and J. Ba, "Adam: A method for stochastic optimization," 2014, *arXiv:1412.6980*. [Online]. Available: <http://arxiv.org/abs/1412.6980>
- [35] L. N. Bohs, B. J. Geiman, M. E. Anderson, S. C. Gebhart, and G. E. Trahey, "Speckle tracking for multi-dimensional flow estimation," *Ultrasonics*, vol. 38, nos. 1–8, pp. 369–375, Mar. 2000.
- [36] S. Fadnes, I. K. Ekroll, S. A. Nyrmes, H. Torp, and L. Lovstakken, "Robust angle-independent blood velocity estimation based on multi-angle speckle tracking and vector Doppler," in *Proc. IEEE Ultrason. Symp.*, Sep. 2014, pp. 337–340.
- [37] F. Mehregan *et al.*, "Doppler vortography: A color Doppler approach to quantification of intraventricular blood flow vortices," *Ultrasound Med. Biol.*, vol. 40, no. 1, pp. 210–221, Jan. 2014.
- [38] T. Ishii, B. Y. S. Yiu, and A. C. H. Yu, "Vector flow visualization of urinary flow dynamics in a bladder outlet obstruction model," *Ultrasound Med. Biol.*, vol. 43, no. 11, pp. 2601–2610, Nov. 2017.
- [39] G.-M. von Reutern *et al.*, "Grading carotid stenosis using ultrasonic methods," *Stroke*, vol. 43, no. 3, pp. 916–921, Mar. 2012.
- [40] B. Y. S. Yiu and A. C. H. Yu, "Least-squares multi-angle Doppler estimators for plane-wave vector flow imaging," *IEEE Trans. Ultrason., Ferroelectr., Freq. Control*, vol. 63, no. 11, pp. 1733–1744, Nov. 2016.
- [41] I. K. Ekroll, J. Avdal, A. Swillens, H. Torp, and L. Lovstakken, "An extended least squares method for aliasing-resistant vector velocity estimation," *IEEE Trans. Ultrason., Ferroelectr., Freq. Control*, vol. 63, no. 11, pp. 1745–1757, Nov. 2016.



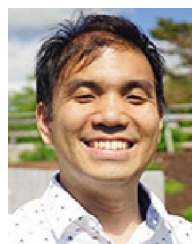
Hassan Nahas (Graduate Student Member, IEEE) received the B.S. degree (*summa cum laude*) in electrical engineering from New York University Abu Dhabi, Abu Dhabi, United Arab Emirates, in 2017. He is currently pursuing the Ph.D. degree in electrical and computer engineering with the University of Waterloo, Waterloo, ON, Canada.

He is currently a member of the Laboratory on Innovative Technology in Medical Ultrasound (LITMUS), University of Waterloo. He has specific research interests in the Doppler ultrasound, flow estimation, and machine learning. He is also broadly interested in biomedical engineering and signal processing, with past involvement in research projects on DNA microarrays and indoor localization.



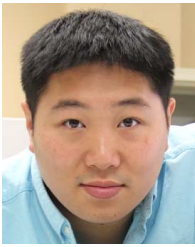
Jason S. Au (Member, IEEE) received the B.Sc. and Ph.D. degrees in kinesiology from McMaster University, Hamilton, ON, Canada, in 2012 and 2017, respectively. His Ph.D. dissertation was on the ultrasound-based analysis of carotid artery longitudinal wall motion.

From 2017 to 2020, through the support of a CIHR Fellowship, he was an Associate Scientist with Laboratory on Innovative Technology in Medical Ultrasound (LITMUS), University of Waterloo, Waterloo, ON, Canada. He recently became an Assistant Professor at the Department of Kinesiology, University of Waterloo. He is a Certified Exercise Physiologist in Canada. He has active research interests in cardiovascular physiology and ultrasound imaging. His research program seeks to better understand how and why the vascular disease is accelerated by complex blood flow and abnormal vascular wall properties.



Takuro Ishii (Member, IEEE) received the B.Eng., M.Eng., and Ph.D. degrees in medical systems engineering from Chiba University, Chiba, Japan, in 2009, 2011, and 2014, respectively.

After completing his Ph.D. degree, he worked for two years at Center for Frontier Medical Engineering, Chiba University. In 2016, he joined The University of Hong Kong, Hong Kong, as a Research Associate. Subsequently, as a JSPS Overseas Research Fellow recipient, he was an Associate Scientist with Laboratory on Innovative Technology in Medical Ultrasound (LITMUS), University of Waterloo, Waterloo, ON, Canada, from 2017 to 2019. Since 2020, he has been an Assistant Professor with Frontier Research Institute for Interdisciplinary Sciences, Tohoku University, Sendai, Japan. He is also a Principal Investigator of the MEXT LEADER Program in Japan. His research interests are in ultrasound flow imaging and urodynamics.

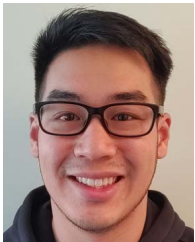


Billy Y. S. Yiu (Member, IEEE) received the B.Eng. degree (Hons.) in medical engineering and the M.Phil. degree in electrical and electronic engineering from The University of Hong Kong, Hong Kong, in 2007 and 2010, respectively, and the Ph.D. degree in electrical and computer engineering from the University of Waterloo, Waterloo, ON, Canada, in 2019.

He was a Research Staff with Biomedical Ultrasound Laboratory, The University of Hong Kong, from 2010 to 2016. He is currently an Associate

Scientist with Laboratory on Innovative Technology in Medical Ultrasound (LITMUS), University of Waterloo. His research interests are in advanced ultrasound imaging techniques and systems.

Dr. Yiu was a recipient of the USE Young Scientist Award, the KSUM Young Investigator Gold Prize Award, and the ASA Biomedical Acoustics Best Student Paper Award.



Adrian J. Y. Chee (Member, IEEE) received the B.Eng. degree in electrical and computer systems engineering from Monash University, Melbourne, VIC, Australia, in 2011, and the Ph.D. degree in mechanical engineering from The University of Hong Kong, Hong Kong, in 2016.

He was a Corporate Intern with Hitachi Central Research Laboratory, Tokyo, Japan, in 2016. He is currently an Associate Scientist with Laboratory on Innovative Technology in Medical Ultrasound, University of Waterloo, Waterloo, ON,

Canada. His research interests are in designing new vascular ultrasound techniques and related experimental tools.



Alfred C. H. Yu (Senior Member, IEEE) received the B.Sc. degree in electrical engineering from the University of Calgary, Calgary, AB, Canada, in 2002, and the M.A.Sc. and Ph.D. degrees in biomedical engineering from the University of Toronto, Toronto, ON, Canada, in 2004 and 2007, respectively.

From 2007 to 2015, he was the Founding Principal Investigator of the Biomedical Ultrasound Laboratory, The University of Hong Kong, Hong Kong. In 2015, he relocated to the Univer-

sity of Waterloo, Waterloo, ON, Canada. He is currently a Full Professor of biomedical engineering with the University of Waterloo, where he is also the Director of the Laboratory on Innovative Technology in Medical Ultrasound (LITMUS). He has long-standing research interests in ultrasound imaging and therapeutics.

Dr. Yu is a Fellow of the American Institute of Ultrasound in Medicine (AIUM). He is also an Elected AdCom Member of the IEEE Ultrasonics, Ferroelectrics, and Frequency Control Society (UFFC-S). He was a recipient of the IEEE Ultrasonics Early Career Investigator Award, the Frederic Lizzi Award, and the Ontario Early Researcher Award. He was the Past Chair of the Medical Ultrasound Group of the IEEE Ultrasonics Symposium. He is also an Associate Editor-in-Chief of the IEEE TRANSACTIONS ON ULTRASONICS, FERROELECTRICS, AND FREQUENCY CONTROL.